1-1-2020

Coupling N2 and CO2 in H2O to synthesize urea under ambient conditions

Chen Chen

Xiaorong Zhu

Xiaojian Wen

Yangyang Zhou

Ling Zhou

See next page for additional authors

Coupling N2 and CO2 in H2O to synthesize urea under ambient conditions

Abstract

© 2020, The Author(s), under exclusive licence to Springer Nature Limited. The use of nitrogen fertilizers has been estimated to have supported 27% of the world's population over the past century. Urea (CO(NH2)2) is conventionally synthesized through two consecutive industrial processes, N2 + H2 → NH3 followed by NH3 + CO2 → urea. Both reactions operate under harsh conditions and consume more than 2% of the world's energy. Urea synthesis consumes approximately 80% of the NH3 produced globally. Here we directly coupled N2 and CO2 in H2O to produce urea under ambient conditions. The process was carried out using an electrocatalyst consisting of PdCu alloy nanoparticles on TiO2 nanosheets. This coupling reaction occurs through the formation of C–N bonds via the thermodynamically spontaneous reaction between *N=N* and CO. Products were identified and quantified using isotope labelling and the mechanism investigated using isotope-labelled operando synchrotron-radiation Fourier transform infrared spectroscopy. A high rate of urea formation of 3.36 mmol g−1 h−1 and corresponding Faradic efficiency of 8.92% were measured at −0.4 V versus reversible hydrogen electrode. [Figure not available: see fulltext.]

Keywords

co2, n2, synthesize, conditions, ambient, coupling, under, urea, h2o

Disciplines

Engineering | Physical Sciences and Mathematics

Publication Details

Chen, C., Zhu, X., Wen, X., Zhou, Y., Zhou, L., Li, H., Tao, L., Li, Q., Du, S., Liu, T., Yan, D., Xie, C., Zou, Y., Wang, Y., Chen, R., Huo, J., Liu, Y., Cheng, J., Su, H., Zhao, X., Cheng, W., Liu, Q., Lin, H., Luo, J., Chen, J., Dong, M., Cheng, K., Li, C. & Wang, S. (2020). Coupling N2 and CO2 in H2O to synthesize urea under ambient conditions. Nature Chemistry, 12 (8), 717-724.

Authors

Chen Chen, Xiaorong Zhu, Xiaojian Wen, Yangyang Zhou, Ling Zhou, Hao Li, Li Tao, Qiling Li, Shiqian Du, Tingting Liu, Dafeng Yan, Chao Xie, Yuqin Zou, Yanyong Wang, Ru Chen, Jia Huo, Yafei Liu, Jun Cheng, Hui Su, Xu Zhao, Weiren Cheng, Qinghua Liu, Hongzhen Lin, Jun Luo, Jun Chen, Mingdong Dong, Kai Cheng, Conggang Li, and Shuangyin Wang

Coupling N_2 and CO_2 in H_2O to synthesis urea under ambient conditions

Chen Chen[1†], Xiaorong Zhu[2†], Xiaojian Wen[3†], Yangyang Zhou[1†], Ling Zhou[1], Hao Li[1], Li Tao[1], Qiling Li[1], Shiqian Du[1], Tingting Liu[1], Dafeng Yan[1], Chao Xie[1], Yuqin Zou[1], Yanyong Wang[1], Ru Chen[1], Jia Huo[1], Yafei Li[2]*, Jun Cheng[3]*, Hui Su[4], Xu Zhao[4], Weiren Cheng[4], Qinghua Liu[4]*, Hongzhen Lin[5], Jun Luo[6], Jun Chen[7]*, Mingdong Dong[8], Kai Cheng[9], Conggang Li[9] and Shuangyin Wang[1]*

[1]State Key Laboratory of Chem/Bio-Sensing and Chemometrics, College of Chemistry and Chemical Engineering, Hunan University, Changsha, Hunan, 410082, P. R. China

[2]College of Chemistry and Materials Science Nanjing Normal University Nanjing, Jiangsu 210023, P. R. China

[3]State Key Laboratory of Physical Chemistry of Solid Surfaces, iChEM, College of Chemistry and Chemical Engineering, Xiamen University, Xiamen, 361005, P. R. China

[4]National Synchrotron Radiation Laboratory, University of Science and Technology of China, Hefei, Anhui, 230029, P. R. China

[5]i-LAB, Suzhou Institute of Nano-Tech and Nano-Bionics, Chinese Academy of Sciences, Suzhou 215123, P. R. China

[6]Tianjin Key Laboratory of Advanced Functional Porous Materials and Center for Electron Microscopy, School of Materials Science and Engineering, Tianjin University of Technology, Tianjin 300384, P. R. China

[7]Intelligent Polymer Research Institute, Australian Institute of Innovative Materials, Innovation Campus, University of Wollongong, Northfields Avenue, Wollongong, NSW 2500, Australia

[8]Interdisciplinary Nanoscience Center, Aarhus University, Denmark

[9]Key Laboratory of Magnetic Resonance in Biological Systems, State Key Laboratory of Magnetic Resonance and Atomic and Molecular Physics, National Center for Magnetic Resonance in Wuhan Collaborative Innovation Center of Chemistry for Life Sciences, Wuhan Institute of Physics and Mathematics, Chinese Academy of Sciences, Wuhan 430071, P. R. China

*Correspondence to: shuangyinwang@hnu.edu.cn; liyafei@njnu.edu.cn; chengjun@xmu.edu.cn; qhliu@ustc.edu.cn; junc@uow.edu.au.

†These authors contributed equally to this work.

Abstract

The use of nitrogen fertilizers has been estimated to have supported 27% of the world's population over the past century. Urea ($CO(NH_2)_2$) is conventionally synthesized through two consecutive industrial processes, $N_2 + H_2 \rightarrow NH_3$ followed by $NH_3 + CO_2 \rightarrow$ urea. Both reactions operate under harsh conditions and consume more than 2% of the world's energy. Urea synthesis consumes approximately 80% of the NH_3 produced globally. Here we directly coupled N_2 and CO_2 in H_2O to produce urea under ambient conditions. The process was carried out using an electrocatalyst consisting of PdCu alloy nanoparticles on TiO_2 nanosheets. This coupling reaction occurs through the formation of C–N bonds via the thermodynamically spontaneous reaction between *N=N* and CO. Products were identified and quantified using isotope labelling and the mechanism investigated using isotope-labelled operando synchrotron radiation Fourier transform infrared spectroscopy. A high urea formation rate of 3.36 mmol g^{-1} h^{-1} and corresponding Faradic efficiency of 8.92% were measured at -0.4 V versus reversible hydrogen electrode.

Over the past century, nitrogen fertilization has supported approximately 27% of the world's population[1]. As urea is one of the most important nitrogen fertilizers with a high nitrogen content, the development of the urea industry is of great significance to meet the demands of an ever-increasing population. Currently, the synthesis of urea is dominated by the reaction of NH_3 and CO_2 under harsh conditions (150-200 °C, 150-250 bar) with large energy consumption. Moreover, complex equipment and multi-cycle synthetic processes are required to enhance the conversion efficiency[2,3]. The production of urea consumes approximately 80% of the global NH_3[4], which is mainly derived from artificial N_2 fixation.

The fixation of earth-abundant N_2 is challenging both scientifically and technologically due to the high inertness of this molecule[5]. The industrial fixation of N_2 and H_2 to obtain ammonia is always dominated by the Haber-Bosch process, operating at a high temperature and high pressure due to the high bonding energy of the N–N triple bond (940.95 kJ mol^{-1}) and consuming approximately 2% of world's energy annually[5-15]. Thus, there have been extensive research activities to reduce the activation energy of the N_2-to-NH_3 reaction under milder conditions[16-19].

Electrocatalytic N_2 fixation under ambient conditions combines the advantages of the utilization of clean energy and protons directly from water[20-23]. However, current research mainly focuses on sole N_2 electrochemical fixation to generate NH_3, and the post treatment of primary products—further applications have seldom been considered[2,3]. Actually, the separation of NH_3 in an aqueous electrolyte and its further purification to obtain gaseous NH_3 with high purity would make the subsequent urea synthesis complicated and unpractical.

For CO_2 fixation, carbon capture and sequestration (CCS) is mainly attributed to the formation of strong covalent bonds (C–N)[24-27], but the high energy consumption, high cost and leakage risk of the captured CO_2 prohibit further application of this method[28]. Compared with the direct electrolysis of CO_2, the electrolysis of CO tends to create multi-carbon products via more efficient C–C coupling[29-31]. On this basis, Jiao and co-workers creatively introduced ammonia as a source of nitrogen to realize C–N coupling and the production of acetamides with a high rate and selectivity (40%) under ambient conditions[32]. In consideration of the hurdles in N_2 and CO_2 fixation and the increasing interest in photo- or electro-driven C–N bond formation[32-34], we hypothesize that the simultaneous electrocatalytic coupling of N_2 and CO_2 would enable the formation of C–N bonds and thus realize the conversion to urea under ambient conditions.

Herein we demonstrate an approach for the electrochemical coupling of N_2 and CO_2 in H_2O to form urea with a carefully designed electrocatalyst consisting of PdCu alloy nanoparticles on TiO_2 nanosheets. Apart from the design of catalysts, the electrolyte utilized also plays the key role in the evaluation of catalytic performance[20,35]. Feng et al. pointed out that the hydrogen evolution reaction (HER) can be efficiently suppressed in a neutral electrolyte to achieve the ammonia synthesis with a high Faradic efficiency[20,36], which is also applicable to this work. Following this guidance, the efficient urea synthesis was achieved with a urea formation rate of 3.36 mmol g^{-1} h^{-1} and a corresponding Faradic efficiency of 8.92% at -0.4 V versus reversible hydrogen electrode (RHE) in a flow cell.

Theoretical calculations are of great significance to the selection of catalysts and the understanding of reaction mechanisms. Medford and co-workers have carried out significant and pioneering research on this topic, developing fundamental understanding of the molecular-scale processes that underlie the important and potentially transformative N_2 and CO_2 reduction processes[37-40]. Inspired by their instructive theory that the carbon radicals on the catalyst surface can interact strongly with N_2 molecules to facilitate the catalytic process[33], possible mechanisms for C–N

bond formation via the thermodynamic spontaneous reaction between *N=N* (the asterisks here indicate the side-on sorption of N_2) and CO were proposed, and the subsequent hydrogenations enable the generation of urea. The formation and evolution of chemical bonds during the electrocatalytic process were monitored by isotope-labelling operando synchrotron radiation Fourier transform infrared spectroscopy (SR-FTIR). The generated urea was identified and quantified based on isotope-labelling experiments.

Results and discussion

Structural characterization of electrocatalysts

TiO_2 nanosheets were prepared as catalyst supports. Defect engineering has been widely adopted to modulate the physicochemical properties of materials[41]. In this work, TiO_2 with oxygen vacancies (OVs) was easily fabricated by treatment of pristine TiO_2 nanosheets under reduction atmosphere at an elevated temperature. The scanning electron microscopy (SEM) images in Supplementary Fig. 1 suggest the maintenance of the nanosheet structure after thermal treatment until the temperature was elevated to 600 °C. The oxygen vacancies were characterized by electron paramagnetic resonance (EPR) spectroscopy, as illustrated in Supplementary Fig. 2, and a symmetric Lorentzian line with a *g* value of 2.003 was obtained[42]. The EPR intensity increased with increasing treatment temperature and reached the highest intensity for TiO_2-400 but dropped for TiO_2-600, indicating that TiO_2-400 has the highest vacancy concentration. The presence of OVs was also confirmed by XPS and Raman spectroscopy (Supplementary Figs. 3 and 4). The formation of OVs could narrow the band gap of TiO_2-400 (Supplementary Fig. 5) but did not change the crystalline phase (Supplementary Fig. 6). However, high-temperature annealing of TiO_2-400 results in a slight decrease in the surface area (Supplementary Fig. 7).

PdCu alloy nanoparticles on pristine TiO_2 and OV-rich TiO_2 nanosheets were fabricated via co-reduction of metal precursors. The SEM images in Supplementary Fig. 8 show the maintenance of the structure of TiO_2 after anchoring the nanoparticles. Typically, the transmission electron microscopy (TEM) image of Pd_1Cu_1/TiO_2-400 displays homogeneous PdCu alloy nanoparticles (approximately 2 nm) loaded onto TiO_2 nanosheets (Fig. 1a). The lattice distance of 0.217 nm in Fig. 1b shows the (111) interplanar distance of the face-centred cubic (FCC) PdCu alloy[43], confirming the successful synthesis of PdCu alloy nanoparticles.

The high-resolution Pd 3d and Cu 2p XPS spectra were carried out to analyse the electronic properties of the PdCu alloy (as presented in Fig. 1c and d). Compared to the binding energy (BE) of Pd $3d_{5/2}$ for Pd/TiO_2 located at 334.9 eV, the BE of Pd_1Cu_1/TiO_2 is shifted slightly to 335.2 eV. Similarly, the BE of Cu $2p_{3/2}$ for Cu/TiO_2 is located at 932.3 eV and shifts to 931.7 eV for Pd_1Cu_1/TiO_2. The shift of the BE is ascribed to the electronic interaction and charge transfer between Pd and Cu[44]. Moreover, the BE of Pd $3d_{5/2}$ for Pd_1Cu_1/TiO_2-400 (Pd_1Cu_1 supported on OV-rich TiO_2) shifts to 335.4 eV, and the BE of Cu $2p_{3/2}$ for Pd_1Cu_1/TiO_2-400 shifts to 931.6 eV, suggesting the enhancement of the interaction between PdCu alloy and OV-TiO_2. For comparison, we also synthesized PdCu nanoparticles with different molar ratios (Supplementary Figs. 10 and 11).

Electrochemical performance towards urea synthesis

Electrochemical urea synthesis by coupling N_2 and CO_2 in H_2O was first carried out in an H-type cell (H-cell, Supplementary Fig. 12). As shown in Supplementary Fig. 13, the diacetyl monoxime method was initially adopted to determine the concentration of urea by measuring the absorbance of the obtained pink solution at 525 nm[45]. The tests were carried out in the range of -0.3 V to -0.8 V versus RHE and the electrochemical performance towards urea synthesis on Pd_1Cu_1/TiO_2 is summarized in Supplementary Fig. 14. A maximum urea formation rate of 0.12 mmol g^{-1} h^{-1} and a corresponding Faradic efficiency of 0.66% were acquired at -0.4 V versus RHE. Beyond this negative potential, the performance towards urea synthesis decreased due to the limited capability for the activation of gaseous molecules. Once the potential decreased below -0.4 V, the enhancement of the competing HER led to the sharp decrease in the urea formation rate and Faradic efficiency[8]. A similar trend was observed for electrocatalysts with various proportions of metal loading.

As illustrated in Supplementary Fig. 14, Pd_1Cu_1/TiO_2 presents the highest urea formation rate at -0.4 V among catalysts with different ratios of Pd and Cu. The sole nitrogen reduction reaction (NRR) and carbon dioxide reduction reaction (CO_2RR) performances in H cells are summarized in Supplementary Figs. 15 and 16 respectively. Pd_1Cu_1/TiO_2 exhibits the highest NH_3 formation rate at -0.4 V due to the synergistic effect derived from a bimetal and optimization of the electronic structure. However, the CO_2RR performance for all catalysts is relatively poor compared to previously reported values[46], which might be attributed to the low metal loads. However, Pd_1Cu_1/TiO_2 also presents higher Faradic efficiencies than mono-metal-loaded samples and a decline in the onset potential. It can be assumed

that the high electrocatalytic activity towards urea synthesis is derived from the simultaneous improvements for NRR and CO_2RR.

PdCu alloy nanoparticles anchored on OV-rich TiO_2 nanosheets were fabricated, and the particle size of the PdCu alloys was controlled in the range of 2–4 nm (Fig. 1a, b and Supplementary Fig. 17). Pd_1Cu_1/TiO_2-400 showed the best performance compared to the other compounds (Supplementary Fig. 18), and a urea formation rate of 0.19 mmol g^{-1} h^{-1} with a corresponding Faradic efficiency of 1.56% was acquired at -0.4 V versus RHE. The CO_2RR performance of Pd_1Cu_1/TiO_2-400 was also improved (Supplementary Fig. 16), indicating the enhanced activation towards CO_2 fixation. Compared to the suppressed CO_2RR performance of Pd_1Cu_1/TiO_2 after the participation of NRR, the CO_2RR performance of Pd_1Cu_1/TiO_2-400 is barely affected due to abundant adsorptive sites and high activation abilities for both N_2 and CO_2. The introduction of OVs enhanced the ability for activation on N_2 and CO_2 for Pd_1Cu_1/TiO_2-400, also facilitating the generation of urea.

Electrochemical measurements for TiO_2-400, Pd/TiO_2-400 and Cu/TiO_2-400 were also carried out (Supplementary Fig. 19). The application of alloy catalysts and optimization of alloy compositions are also crucial to the C–C coupling in CO_2RR process[47]. The urea formation rate of Pd_1Cu_1/TiO_2-400 was obviously higher than that of the substrate and sample with a single metal anchored; thus, the effect of the alloy structure on the catalytic performance was further demonstrated.

The support utilized here also plays a key role in boosting the electrocatalytic performance for urea synthesis. Carbon black (XC72R) with higher conductivity also served as the support for metal loading. Nevertheless, Pd_1Cu_1/XC72R exhibits a low urea formation rate (Supplementary Fig. 20), which might be ascribed to the weakened interaction between the metal and carbon support. The TiO_2 has been reported to stabilize the intermediates to promote CO_2RR compared with carbon support[48], and the application of TiO_2 especially the OV-rich one is crucial to promote the urea synthesis in this work. Thus the catalytic activity towards urea synthesis is due to the optimized electronic structure and the strong interaction between the metal and support.

The utilization of flow cells has been reported to improve electrocatalytic performance towards NRR[12,49] and CO_2RR[46-48,50,51] respectively and was introduced to boost the performance for electrochemical urea synthesis in this work. With contrast to the tests in conventional H cells, the tests in flow cells (Supplementary Fig. 21) possess efficient mass transport[50] and higher fraction of coverage on electrode for

gaseous reactants[49,52], resulting in improved performance towards gas-consumption reactions.

Electrochemical tests in the flow cell were conducted, and the liquid products were quantified by ^{1}H nuclear magnetic resonance (NMR) spectroscopy based on the linear relationship between concentrations and integral area (Supplementary Figs. 22-24). The gaseous products were quantified by gas chromatography (GC). Compared with the test in the H cell, in the flow cell, Pd_1Cu_1/TiO_2-400 exhibited a higher ammonia formation rate (2.91 mmol g^{-1} h^{-1}) at -0.4 V versus RHE and presented a descending trend along with increasing applied negative potential (Fig. 2b). Furthermore, the CO_2RR performance was also improved, as shown in Fig. 2c. As predicted, the urea formation rates in flow cells were significantly enhanced, and the highest yield rate of 3.36 mmol g^{-1} h^{-1} was reached at -0.4 V. The Faradic efficiencies and corresponding current densities for tests in a CO_2- and N_2- saturated electrolyte are summarized in Fig. 2e. The results exhibit a lower ammonia yield at -0.4 V than the NRR results in Fig. 2b, indicating a modulated reaction pathway or the consumption of NRR intermediates to produce urea. Although the reaction was always dominated by hydrogen evolution, the catalyst also exhibited a desirable urea formation rate (3.36 mmol g^{-1} h^{-1}) and relatively high Faradic efficiency (8.92%) compared to the low ammonia yield at -0.4 V.

To further boost the electrocatalytic performance[53], tests with increasing concentrations of electrolyte were conducted at -0.4 V. An improvement of urea synthesis was observed with the increase in $KHCO_3$ concentration, and the highest yield rate of 3.76 mmol g^{-1} h^{-1} with a corresponding Faradic efficiency of 9.43% was achieved (Supplementary Fig. 25). When the electrolyte concentration and the gas flow rate remain constant, the yield rate in this cell might be affected by the flow rate of the electrolyte[50]. Thus, control experiments with various electrolyte flow rates (1, 5, 10, 15, 20 and 25 mL min^{-1}) were performed. The urea formation rate increased as the flow rate increased, possibly attributing to the further enhanced mass transfer and removal of products rapidly. The urea formation rate reached its limit (4.00 mmol g^{-1} h^{-1}) at a rate of 20 mL min^{-1}. A similar trend was also observed for the Faradic efficiency.

As the chemisorption of N_2 is the initial step towards NRR, the N_2 chemisorption ability of the catalysts was measured by temperature-programmed desorption (TPD) with a mass detector. The results in Fig. 3a indicate that TiO_2-400 has weak N_2 chemisorption. After anchoring metal nanoparticles, the catalysts exhibit significant enhancement in the chemisorption of N_2, particularly for the alloy state. In addition to

the enhanced intensity, peak shifts also appeared. The Cu/TiO_2-400 spectrum presents a peak located at 234 °C; the peak shifts to 258 °C for Pd/TiO_2-400, and an additional peak at 360 °C appears. The shift of the peak to a higher temperature indicates higher binding energies and stronger chemical adsorptions of gas molecules[22].

Owing to the electronic interaction of a bimetal, the TPD peaks further shift to higher temperatures (270 °C and 380 °C), indicating the superior chemical adsorption ability in the alloy state. Likewise, Pd_1Cu_1/TiO_2-400 also presents the highest ability for chemisorption of CO_2 (Fig. 3b). More importantly, the competitive sorption of CO_2 and N_2 was carried out, and only negligible shifts for all peak positions were observed, meaning benign competition existed in the chemical adsorption of CO_2 and N_2, resulting in efficient urea synthesis.

Experimental mechanistic studies

To gain an in-depth understanding of the catalytic process, cutting-edge operando SR-FTIR was performed under working conditions[54]. The effective infrared signal is shown by a transmission mode in the FTIR results, which reveals that the negative peaks in the spectra represent the vibration absorption bands of key intermediates during the catalytic process.

As shown in Fig. 4, the SR-FTIR signals are clearly potential dependent. For the Pd_1Cu_1/TiO_2-400 electrode at a low potential of -0.15 V, the vibration bands for NH, NH_2, and COOH, were not detected, suggesting that the electroreduction of N_2 and CO_2 did not occur. When a potential of -0.20 V was applied, new weak vibration bands at ~3171, ~3291 and ~3441 cm^{-1} that are assigned to the stretching vibrations of NH_2 and NH appeared (Fig. 4a)[21,55,56]. As the potential increased to -0.25 V, new weak vibration bands at ~1699 and 1177-1314 cm^{-1} assigned to the stretching vibrations of C=O and C–O were observed (Fig. 4b)[57], respectively, implying that the slow electroreduction of CO_2 also occurred. Along with increasing potential (negative than -0.30 V), the vibration intensities of NH_2, NH and C=O gradually increased. At the same time, a stretching vibration of C–N at ~1449 cm^{-1} emerged (Fig. 4b)[56,58] as the key bond for the formation of urea at -0.30 V. It is of note that these vibration bands reached their peak values at -0.40 V, which is consistent with the electrochemical performance measurements. The SR-FTIR results of the control experiments are also summarized in Supplementary Fig. 26. The vibration band intensities of NH and NH_2 for urea synthesis on Pd_1Cu_1/TiO_2-400 are higher than those of the sole NRR test and obviously higher than the test results for the CO_2RR, consistent with the electrochemical test results. Moreover, the IR signals of

Pd_1Cu_1/TiO_2-400 are significantly superior to those of the support (TiO_2-400), indicating that the electrocatalytic active source is mainly PdCu alloy.

To further deepen the above analysis, isotope-labelling operando SR-FTIR experiments were conducted for the Pd_1Cu_1/TiO_2-400 catalyst under applied potentials of -0.15 to -0.45 V versus RHE with $^{15}N_2$ and/or $^{13}CO_2$ as the feeding gases. As seen from the isotope-labelling measurements in Fig. 4c and d, the vibrations of $^{15}NH_2$, ^{15}NH and $^{13}C{=}O$ are shifted towards lower wavenumbers by 20–30 cm^{-1}, and the vibration of $^{13}C–^{15}N$ is evidently shifted towards lower wavenumbers by 34 cm^{-1}. These shifts are attributed to the isotope effect[54], confirming the electroreduction of N_2 and CO_2 feeding gases during the reaction. The control experiments in Supplementary Figs. 27-29 further illustrate the possible occurrences of the NRR, the CO_2RR and urea synthesis on Pd_1Cu_1/TiO_2-400.

The electrochemical test on the bare glassy carbon electrode excluded the possibility of C–N bond formation via the interaction between the carbon-containing electrode support and nitrogen gas (Supplementary Fig. 30). Summarizing the above results, it can be seen that N_2 activation started at -0.20 V, and as the potential was increased to -0.25 V, the intermediate of *COOH attributed to CO_2 activation was observed. The above results could serve as evidence for C–N bond formation and the occurrence of electrocatalytic processes.

Theoretical mechanistic studies

Density functional theory (DFT) calculations were carried out to further investigate the microscopic mechanism of this Pd-Cu system using the computational hydrogen electrode (CHE)[59] model, which has been previously proven to be applicable to N_2 and CO_2 reduction reactions on metal surfaces.

Urea production starts with N_2 adsorption on the Pd-Cu surface with a side-on configuration. The side-on adsorption facilitates back feed of electrons from the d orbitals of Pd and Cu to the π^* orbitals of N_2, reducing the N–N bond order[60,61]. According to the TPD results, the gas adsorption ability of catalyst has been significantly enhanced, attributing to the support effect and bimetal structure mostly. The existence of activated N_2 molecules can further promote CO_2RR to CO on adjacent metal sites. Supplementary Fig. 31 presents the optimized geometry of the key intermediate *COOH with and without the neighbouring N_2. The corresponding free energy diagram indicates that the limiting potential of the CO_2RR process can be reduced from 0.22 V to 0.12 V in the presence of co-adsorbed N_2 molecules.

Once the CO was released, the *N=N* showed a strong effect on the CO due to the matched molecular orbitals. After binding with CO and formation of the tower-like urea precursor *NCON*, the N–N bond was elongated from 1.14 Å to 1.58 Å, and the energy barrier of this process (presented in Fig. 5b) had a moderate E_a value (approximately +0.79 eV) on the Pd-Cu surface. From a thermodynamic prospective, *NCON* formation is exothermic, and the free energy change was calculated to be -0.89 eV. The competition reaction of *NNH formation is highly endothermic with an energy input of +0.90 eV. Thus, the release of the side product NH_3 can be greatly suppressed, and the positive ΔG^*_{NNH} provides an important premise for the high urea selectivity of Pd-Cu systems. In all, the generation of intermediates (*NCON*) via activating N_2 is thermodynamically and kinetically feasible, acting as the key factor for the effective urea production.

Based on the above results, the production of CO at -0.3 V or -0.4 V versus RHE in this co-electrocatalysis system is possible; but the subsequent reaction could prohibit the release of CO macroscopically. Thus, the high yield rate of urea is mainly derived from the mutual promotion between the NRR and the CO_2RR and both optimized reaction pathways. Furthermore, the amount of CO needs to be well controlled, as once the potential exceeds -0.4 V, the decline in the yield rate for urea is ascribed to the excessive release of CO and its occupation of adsorptive sites for N_2 and CO_2 to some extent.

The hydrogenation of N can be assisted by the carbonyl functional group. The H atoms prefer to add to the N atom directly connected with Cu to break the single N–N bond. The *NCONH structural integrity can be well maintained after the first hydrogen atoms are added to the Cu-bound N atom due to the comparable Cu–N and C–N bond strengths. This can be further proven by the clear electron redistribution between the Pd and Cu atoms (Supplementary Fig. 32). The electron delocalization of Cu is much smaller than that of Pd, and the less positively charged Cu atoms with weaker Cu–N bonds are more favourable for *NCON* hydrogenation and *NCONH stabilization. When H is added to *NCONH, two reaction pathways may occur. The distal product *$NCONH_2$ was +0.14 eV more stable than the alternative product *NHCONH. The third proton-coupled electron transfer process was energy demanding and was the potential-limiting step of urea production. The limiting potential was +0.64 V and +0.78 V for the distal and alternative mechanisms, respectively. The subsequent reduction steps are exothermic, and the urea can be easily desorbed from the Pd-Cu surfaces.

A detailed reaction mechanism with the most stable geometries structures of the reactants, intermediates, and products throughout urea formation is listed in Supplementary Fig. 32. The computational results reveal that the presence of $*N_2$ can facilitate CO_2 reduction, and the reduced CO can further react with $*N_2$ to form urea with ultrahigh activity and selectivity.

Conclusions

The fixation of gaseous molecules, particularly that of N_2, has attracted extreme attention but is challenging due to the intrinsic inertness of this molecule. This work not only focuses on the reduction of N_2 to NH_3 but, more importantly, aims at the electrocatalytic coupling of N_2 and CO_2 simultaneously to realize the green synthesis of urea under ambient conditions. With the rational design of the electrocatalyst, enhanced chemisorption and catalytic reactions of N_2 and CO_2 were realized on the alloy state (Pd_1Cu_1/TiO_2-400). The electrocatalytic process was monitored by operando SR-FTIR, and the products were identified and quantified via isotope-labelling experiments. Furthermore, possible mechanisms for urea synthesis were proposed. This work successfully realized C–N bond formation and urea generation under ambient conditions, providing a novel pathway for the fixation of inert N_2 and CO_2 (Supplementary Fig. 33).

References

1. Erisman, J. W., Sutton, M. A., Galloway, J., Klimont, Z. & Winiwarter, W. How a century of ammonia synthesis changed the world. *Nat. Geosci.* **1**, 636-639 (2008).
2. Barzagli, F., Mani, F. & Peruzzini, M. From greenhouse gas to feedstock: formation of ammonium carbamate from CO_2 and NH_3 in organic solvents and its catalytic conversion into urea under mild conditions. *Green Chem.* **13**, 1267-1274 (2011).
3. Pérez-Fortes, M., Bocin-Dumitriu, A. & Tzimas, E. CO_2 utilization pathways: techno-economic assessment and market opportunities. *Energy Procedia* **63**, 7968-7975 (2014).
4. Giddey, S., Badwal, S. P. S. & Kulkarni, A. Review of electrochemical ammonia production technologies and materials. *Int. J. Hydrogen Energ.* **38**, 14576-14594 (2013).
5. Service, R. F. Chemistry. New recipe produces ammonia from air, water, and sunlight. *Science* **345**, 610 (2014).
6. Chen, C. et al. B-N pairs enriched defective carbon nanosheets for ammonia synthesis with high efficiency. *Small* 1805029 (2019).
7. Licht, S. et al. Ammonia synthesis by N_2 and steam electrolysis in molten

hydroxide suspensions of nanoscale Fe_2O_3. *Science* **345**, 637-640 (2014).

8. Shi, M. M. et al. Au sub-nanoclusters on TiO_2 toward highly efficient and selective electrocatalyst for N_2 conversion to NH_3 at ambient conditions. *Adv. Mater.* **29**, 1606550 (2017).
9. Bao, D. et al. Electrochemical reduction of N_2 under ambient conditions for artificial N_2 fixation and renewable energy storage using N_2/NH_3 cycle. *Adv. Mater.* **29**, 1604799 (2017).
10. Chen, G. F. et al. Ammonia electrosynthesis with high selectivity under ambient conditions via a Li^+ incorporation strategy. *J. Am. Chem. Soc.* **139**, 9771-9774 (2017).
11. Li, S. J. et al. Amorphizing of Au nanoparticles by CeO_x-RGO hybrid support towards highly efficient electrocatalyst for N_2 reduction under ambient conditions. *Adv. Mater.* **29**, 1700001 (2017).
12. Chen, S. et al. Electrocatalytic synthesis of ammonia at room temperature and atmospheric pressure from water and nitrogen on a carbon-nanotube-based electrocatalyst. *Angew. Chem. Int. Ed.* **56**, 2699-2703 (2017).
13. Lan, R., Irvine, J. T. & Tao, S. Synthesis of ammonia directly from air and water at ambient temperature and pressure. *Sci. Rep.* **3**, 1145 (2013).
14. Van der Ham, C. J., Koper, M. T. & Hetterscheid, D. G. Challenges in reduction of dinitrogen by proton and electron transfer. *Chem. Soc. Rev.* **43**, 5183-5191 (2014).
15. Guo, C., Ran, J., Vasileff, A. & Qiao, S. Z. Rational design of electrocatalysts and photo (electro) catalysts for nitrogen reduction to ammonia (NH_3) under ambient conditions. *Energy Environ. Sci.* **11**, 45-56 (2018).
16. Foster, S. L. et al. Catalysts for nitrogen reduction to ammonia. *Nat. Catal.* **1**, 490 (2018).
17. Li, H., Shang, J., Ai, Z. & Zhang, L. Efficient visible light nitrogen fixation with BiOBr nanosheets of oxygen vacancies on the exposed {001} facets. *J. Am. Chem. Soc.* **137**, 6393-6399 (2015).
18. Wang, S. et al. Light-switchable oxygen vacancies in ultrafine Bi_5O_7Br nanotubes for boosting solar-driven nitrogen fixation in pure water. *Adv. Mater.* **29**, 1701774 (2017).
19. Zheng, J. et al. Photoelectrochemical synthesis of ammonia on the aerophilic-hydrophilic heterostructure with 37.8% efficiency. *Chem* **5**, 1-17 (2019).
20. Wang, J. et al. Ambient ammonia synthesis via palladium-catalyzed electrohydrogenation of dinitrogen at low overpotential. *Nat. Commun.* **9**, 1795 (2018).

21. Yao, Y., Zhu, S., Wang, H., Li, H. & Shao, M. A spectroscopic study on the nitrogen electrochemical reduction reaction on gold and platinum surfaces. *J. Am. Chem. Soc.* **140**, 1496-1501 (2018).
22. Geng, Z. et al. Achieving a record-high yield rate of 120.9 for N_2 electrochemical reduction over Ru single-atom catalysts. *Adv. Mater.* **30**, 1803498 (2018).
23. Yu, X. et al. Boron-doped graphene for electrocatalytic N_2 reduction. *Joule* **2**, 1610-1622 (2018).
24. Inagaki, F., Matsumoto, C., Iwata, T. & Mukai, C. CO_2-selective absorbents in air: reverse lipid bilayer structure forming neutral carbamic acid in water without hydration. *J. Am. Chem. Soc.* **139**, 4639-4642 (2017).
25. McDonald, T. M., D'Alessandro, D. M., Krishna, R. & Long, J. R. Enhanced carbon dioxide capture upon incorporation of N,N′-dimethylethylenediamine in the metal-organic framework CuBTTri. *Chem. Sci.* **2**, 2022-2028 (2011).
26. Flaig, R. W. et al. The chemistry of CO_2 capture in an amine-functionalized metal-organic framework under dry and humid conditions. *J. Am. Chem. Soc.* **139**, 12125-12128 (2017).
27. Planas, N. et al. The mechanism of carbon dioxide adsorption in an alkylamine-functionalized metal-organic framework. *J. Am. Chem. Soc.* **135**, 7402-7405 (2013).
28. Zhu, D. D., Liu, J. L. & Qiao, S. Z. Recent advances in inorganic heterogeneous electrocatalysts for reduction of carbon dioxide. *Adv. Mater.* **28**, 3423-3452 (2016).
29. Jouny, M., Luc, W. & Jiao, F. High-rate electroreduction of carbon monoxide to multi-carbon products. *Nat. Catal.* **1**, 748-755 (2018).
30. Luc, W. et al. Two-dimensional copper nanosheets for electrochemical reduction of carbon monoxide to acetate. *Nat. Catal.* **2**, 423-430 (2019).
31. Jouny, M., Hutchings, G. S. & Jiao, F. Carbon monoxide electroreduction as an emerging platform for carbon utilization. *Nat. Catal.* **2**, 1062-1070 (2019).
32. Jouny, M. et al. Formation of carbon-nitrogen bonds in carbon monoxide electrolysis. *Nat. Chem.* **11**, 846-851 (2019).
33. Comer, B. M. et al. The role of adventitious carbon in photo-catalytic nitrogen fixation by titania. *J. Am. Chem. Soc.* **140**, 15157-15160 (2018).
34. Srinivas, B., Kumari, V. D., Sadanandam, G., Subrahmanyam, C. H. M. & De, B. R. Photocatalytic synthesis of urea from in situ generated ammonia and carbon dioxide. *Photochem. Photobiol.* **88**, 233-241 (2012).
35. Wang, J. et al. A bifunctional catalyst for efficient dehydrogenation and electro-oxidation of hydrazine. *J. Mater. Chem. A* **6**, 18050-18056 (2018).
36. Hu, L. et al. Ambient electrochemical ammonia synthesis with high selectivity on Fe/Fe oxide catalyst. *ACS Catal.* **8**, 9312-9319 (2018).
37. Comer, B. M. et al. Prospects and challenges for solar fertilizers. *Joule* **3**, 1578-1605 (2019).
38. Medford, A. J. et al. Assessing the reliability of calculated catalytic ammonia synthesis rates. *Science* **345**, 197-200 (2014).

39. Duyar, M. S. et al. A highly active molybdenum phosphide catalyst for methanol synthesis from CO and CO_2. *Angew. Chem.* **130**, 15265-15270 (2018).
40. Andersen, M. et al. Scaling-relation-based analysis of bifunctional catalysis: the case for homogeneous bimetallic alloys. *ACS Catal.* **7**, 3960-3967 (2017).
41. Yan, D., Li, H., Chen, C., Zou, Y. & Wang, S. Defect engineering strategies for nitrogen reduction reactions under ambient conditions. *Small Methods* 1800331 (2018).
42. Wan, J. et al. Defect effects on TiO_2 nanosheets: Stabilizing single atomic site Au and promoting catalytic properties. *Adv. Mater.* **30**, 1705369 (2018).
43. Qiu, Y. et al. BCC-phased PdCu alloy as a highly active electrocatalyst for hydrogen oxidation in alkaline electrolytes. *J. Am. Chem. Soc.* **140**, 16580-16588 (2018).
44. Shi, M. M. et al. Anchoring PdCu amorphous nanocluster on graphene for electrochemical reduction of N_2 to NH_3 under ambient conditions in aqueous solution. *Adv. Energy Mater.* **8**, 1800124 (2018).
45. Rahmatullah, M. & Boyde, T. R. C. Improvements in the determination of urea using diacetyl monoxime; methods with and without deproteinisation. *Clin. Chim. Acta* **107**, 3-9 (1980).
46. Ma, S. et al. Electroreduction of carbon dioxide to hydrocarbons using bimetallic Cu-Pd catalysts with different mixing patterns. *J. Am. Chem. Soc.* **139**, 47-50 (2016).
47. Hoang, T. T. H. et al. Nanoporous copper-silver alloys by additive-controlled electrodeposition for the selective electroreduction of CO_2 to ethylene and ethanol. *J. Am. Chem. Soc.* **140**, 5791-5797 (2018).
48. Ma, S., Lan, Y., Perez, G. M. J., Moniri, S. & Kenis, P. J. A. Silver supported on titania as an active catalyst for electrochemical carbon dioxide reduction. *ChemSusChem* **7**, 866-874 (2014).
49. Cook, R. L. & Sammells, A. F. Ambient temperature gas phase electrochemical nitrogen reduction to ammonia at ruthenium/solid polymer electrolyte interface. *Catal. Lett.* **1**, 345-349 (1988).
50. Billy, J. T. & Co, A. C. Experimental parameters influencing hydrocarbon selectivity during the electrochemical conversion of CO_2. *ACS Catal.* **7**, 8467-8479 (2017).
51. Albo, J. & Irabien, A. Cu_2O-loaded gas diffusion electrodes for the continuous electrochemical reduction of CO_2 to methanol. *J. Catal.* **343**, 232-239 (2016).
52. Wang, H. et al. Selective electrochemical reduction of nitrogen to ammonia by adjusting the three-phase interface. *Research* **2019**, 1401209 (2019).
53. Hao, Y. et al. Promoting nitrogen electroreduction to ammonia with bismuth nanocrystals and potassium cations in water. *Nat. Catal.* **2**, 448 (2019).
54. Cheng, W. R. et al. Lattice-strained metal-organic-framework arrays for bifunctional oxygen electrocatalysis. *Nat. Energy* **4**, 115-122 (2019).
55. Coleman, M. M., Lee, K. H., Skrovanek, D. J. & Painter, P. C. Hydrogen bonding

in polymers. 4. Infrared temperature studies of a simple polyurethane. *Macromolecules* **19**, 2149-2157 (1986).

56. Manivannan, M. & Rajendran, S. Investigation of inhibitive action of urea-Zn^{2+} system in the corrosion control of carbon steel in sea water. *Int. J. Engr. Sci. Technol.* **3**, 8048-8060 (2011).

57. Buong, W. C., Nor, A. I., Wan, M. Z. W. Y. & Mohd, Z. H. Poly(lactic acid)/poly(ethylene glycol) polymer nanocomposites: effects of graphene nanoplatelets. *Polymers* **6**, 93-104 (2014).

58. Daramola, M. O., Nicola, W. & Jacob, M. N. Effect of the presence of water-soluble amines on the carbon dioxide (CO_2) adsorption capacity of amine-grafted poly-succinimide (PSI) adsorbent during CO_2 capture. *Energy Procedia* **86**, 90-105 (2016).

59. Nørskov, J. K. et al. Origin of the overpotential for oxygen reduction at a fuel-cell cathode. *J. Phys. Chem. B* **108**, 17886-17892 (2004).

60. Honkala, K. et al. Ammonia synthesis from first-principles calculations. *Science* **307**, 555-558 (2005).

61. Duan, H. et al. Molecular nitrogen promotes catalytic hydrodeoxygenation. *Nat. Catal.* **2**, 1078-1087 (2019).

Acknowledgments

The authors acknowledge support from the National Natural Science Foundation of China (Grant No. 21825201, U19A2017, U1932212) and ARC DP170102320.

Author contributions

S.W. conceived the project. C.C. and Y.Z. carried out most of the experiments and co-wrote the manuscript. X.Z., Y. L., X.W. and J.C. performed the theoretical calculations. Q.L., H.S., X.Z. and W.C. carried out the isotope-labelling operando SR-FTIR measurements. L.Z., L.T., H.L., Q.L., S.D., T.L., D.Y. and C.X. conducted part of the synthesis of catalysts and characterizations. Y.Z., Y.W., R.C. and J.H. analyzed the data. H.L., J.L., J.C. and M.D. performed the partial characterizations of materials. K.C. and C.L. performed the collection and analysis of NMR spectra. All authors discussed the results and commented on the manuscript.

Competing interests

The authors declare no conflict of interest.

Additional information

Supplementary information is available for this paper. Reprints and permissions information is available at www.nature.com/reprints. Correspondence and requests for materials should be addressed to S.W.

Figure captions

Figure 1 | Morphology and high-resolution XPS spectra of catalysts. (a) TEM image of Pd_1Cu_1/TiO_2-400; the inset shows the distribution of the PdCu nanoparticles. The scale bar is 25 nm. (b) High-resolution TEM image (HRTEM) of Pd_1Cu_1/TiO_2-400. The scale bar is 2 nm. (c) Pd 3d XPS spectra of Pd/TiO_2, Pd_1Cu_1/TiO_2 and Pd_1Cu_1/TiO_2-400. (d) Cu 2p XPS spectra of Cu/TiO_2, Pd_1Cu_1/TiO_2 and Pd_1Cu_1/TiO_2-400.

Figure 2 | Evaluation of the electrocatalytic performance of Pd_1Cu_1/TiO_2-400 in a flow cell. (a) Schematic diagram for urea synthesis. The gray, navy, red, and white spheres represent the C, N, O, and H atoms, respectively. (b) Ammonia synthesis with N_2 as the feeding gas at various potentials. (c) CO production with CO_2 as the feeding gas. (d) Urea generation with CO_2 and N_2 as feeding gases. (e) The Faradic efficiencies and the total current densities for all products at various potentials. (f) Mass spectra of derivation of urea with unmarked gas and isotope-labelling gas as feeding gases. The error bars represent the s.d. for at least three independent measurements.

Figure 3 | Sorption of gaseous molecules on catalysts. (a) N_2-TPD spectra of TiO_2-400, Pd/TiO_2-400, Cu/TiO_2-400 and Pd_1Cu_1/TiO_2-400. (b) CO_2-TPD spectra of TiO_2-400, Pd/TiO_2-400, Cu/TiO_2-400 and Pd_1Cu_1/TiO_2-400. (c) Competitive chemisorption of N_2 (red) and CO_2 (blue) on TiO_2-400 and Pd_1Cu_1/TiO_2-400.

Figure 4 | Isotope-labelling operando SR-FTIR spectroscopy measurement results. (a) IR signal in the range of 2750-3600 cm^{-1} and (b) IR signal in the range of 1100-1800 cm^{-1} under various potentials for Pd_1Cu_1/TiO_2-400 during the electrocoupling of N_2 and CO_2. Isotope-labelling IR signals in the range of 2750-3600 cm^{-1} (c) and in the range of 1100-1800 cm^{-1} (d) at -0.40 V versus RHE for Pd_1Cu_1/TiO_2-400 during the electrocoupling of $^{15}N_2$ and/or $^{13}CO_2$ processes.

Figure 5 | Theoretical calculation results for urea synthesis. (a) Free energy diagram of urea production. (b) The reaction pathway of *NCON* formation. The structures of

the initial, transition and final states along with the *NCON* formation were also presented. The green, orange, blue, red, gray, and white balls represent Pd, Cu, N, O, C, and H atoms, respectively. The line is simply to guide the eye.

Methods

Materials fabrication. The synthesis of TiO_2 nanosheets is described elsewhere[42]. TiO_2 nanosheets anchoring with PdCu alloy nanoparticles was fabricated via co-reduction of metal precursors by sodium borohydride. Typically, 30 mg of TiO_2 nanosheets was dispersed into 20 ml of distilled water with ultrasonic treatment for 30 min. Then, air in the solution was expelled by argon gas flow. After that, the dissolved $PdCl_2$ (3.6 mmol) and $CuCl_2 \cdot 2H_2O$ (3.6 mmol) were added dropwise to the dispersion of TiO_2. Subsequently, 50 mg of $NaBH_4$ in water (5 mL) was added dropwise to the above solution for 30 min. After reaction for another 2 h, the obtained powder was separated with centrifugation and washed with distilled water and ethanol for several times, and then dried. More details were afforded in the Supplementary Table 1. The TiO_2 nanosheets were thermal treated in reduction atmosphere (reduction gas contains 10 vol.% hydrogen and 90 vol.% argon) for 2 h at various temperatures to achieve the fabrication of defective TiO_2. PdCu alloy anchoring on defective TiO_2 nanosheets was synthesized via the same synthetic procedures as for the fabrication of Pd_1Cu_1/TiO_2 except that the support was instead by defective TiO_2 nanosheets. Pd_1Cu_1/XC72R was prepared by the same synthetic procedures as well except the utilization of carbon black (XC72R) as the support.

Materials characterization. The morphology was analyzed by field emission SEM and TEM (FEI Tecnai G2 F20). XRD measurements were performed on a D8 ADVANCE X-ray diffractometer (Bruker). The EPR measurements were carried out on a JEOL JES-FA200 spectrometer and the XPS analysis was conducted on with an ESCALAB 250 Xi X-ray photoelectron spectrometer. Diffuse reflectance spectra (DRS) were acquired using a Cary 5000 spectrophotometer fitted with an integrating sphere attachment from 200-800 nm with $BaSO_4$ as the reference. The Raman spectra of catalysts were acquired on a RENISHAW inVia Raman Microscope. The specific surface areas of the catalysts were measured on a JW-BK200C (JWGB SCI. & TECH) Specific Surface Area and Aperture Analyzer. The gaseous products for ECR were quantified on a GC-2014C SHIMADZU gas chromatograph. The ^1H NMR spectra were measured on an Ascend^{TM} 600 NMR spectrometer equipped with an ultralow temperature probe. The mass spectra were collected on a GCMS-QP2020NX SHIMADZU instrument.

TPD measurements. TPD measurements were carried out on an AutoChem 2920 instrument. For the measurement of N_2-TPD, 150 mg of catalyst powder was placed in a glass tube and pretreated by the He gas flow at 150 °C for 1 h, and then cooled down to 50 °C. The adsorption of N_2 was conducted in N_2 (99.999%) gas flow for 3 h at 50 °C. After purging with He (99.999%) gas for 0.5 h to remove the residual N_2, the sample was heated from 50 °C to 400 °C with a rate of 10 °C min^{-1}. The TPD signal was recorded using a MS detector (M/Z=28). The CO_2-TPD measurement was the same as the measurement of N_2-TPD except that the absorbent was instead by CO_2 (99.999%) and the TPD signal was recorded using a MS detector (M/Z=44). The competitive chemisorptions of N_2 and CO_2 were measured with the absorbent of mixing N_2 and CO_2 (1:1, v/v). The TPD signal was recorded using a MS detector and the data of M/Z=28 and M/Z=44 were collected.

Operando SR-FTIR measurements. Operando synchrotron radiation FTIR measurements were made at the infrared beamline BL01B of National Synchrotron Radiation Laboratory (NSRL, China) through a homemade top-plate cell reflection IR setup with a ZnSe crystal as the infrared transmission window (cutoff energy of ~625 cm^{-1}).This end-station was equipped with an FTIR spectrometer (Bruker 66v/s) with a KBr beam splitter and various detectors (herein a liquid nitrogen cooled MCT detector was used) coupled with an IR microscope (Bruker Hyperion 3000) with a 16× objective, and can provide infrared spectroscopy measurement with a broad range of 15-4000 cm^{-1} as well as a high spectral resolution of 0.25 cm^{-1}. The catalyst electrode is tightly pressed against the ZnSe crystal window with a micron-scale gap in order to reduce the loss of infrared light. To ensure the quality of the obtained SR-FTIR spectra, the apparatus adopts a reflection mode with a vertical incidence of infrared light. Each infrared absorption spectrum was acquired by averaging 514 scans at are solution of 2 cm^{-1}. All infrared spectral acquisitions were carried out after a constant potential was applied to the catalysts electrode for 20 min. The background spectrum of the catalyst electrode was acquired at an open-circuit voltage before each systemic measurement, and the measured potential ranges of the electrocoupling reaction were -0.15 to -0.45 V with an interval of 0.05 V. The in situ electrochemical cell is shown in Supplementary Fig. 34.

Electrochemical characterization. The electrochemical test in H-type cell is carried out on a CHI 660E electrochemical station in a three-electrode system. The pre-treated Nafion 117 membrane (Dupont) served as the separator and the electrolyte used in this work is 0.1 M $KHCO_3$. 2 mg of catalyst were dispersed in 950 μL of ethanol and 50 μL of Nafion (5 wt% aqueous solution) with sonication for 30 min to

form a homogenous ink. Then, 100 μL of catalyst ink were loaded onto a piece of carbon paper (HESEN Company) and dried naturally to obtain the working electrode, the geometric area of working electrode is 1×1 cm^2 and the catalyst loading is 0.2 mg cm^{-2}. The reference electrode is an Ag/AgCl electrode containing saturated KCl solution and a carbon rod is served as the counter electrode. Before electrochemical tests, the cathode part of electrolyte was purged with corresponding gases for pre-saturation. After that, the flow rate was maintained at 30 mL min^{-1} during the catalytic process. The provided applied potentials are against an Ag/AgCl (saturated KCl solution) and converted to the RHE reference scale using E_{RHE}= $E_{Ag/AgCl}$+0.0591×pH+0.197. The pH value is 6.8 for CO_2 saturated electrolyte or N_2 and CO_2 saturated electrolyte, and it is 8.3 for sole N_2 saturated 0.1 M $KHCO_3$ aqueous solution. The feeding gas contains 50 vol.% N_2 and 50 vol.% CO_2 for electrochemical urea synthesis, and this gas ratio is also adopted for isotope-labelling experiments and operando SR-FTIR measurements.

The flow cell configuration is depicted in Supplementary Fig. 21, consisting of a working electrode, anion exchange membrane and nickel foam anode. 0.8 mg of catalyst was deposited on the top side of carbon paper with microporous layer. The combined catalyst and working electrode, anion exchange membrane and nickel anode were then positioned and clamped together using polytetrafluoroethylene (PTFE) spacers such that a liquid electrolyte could be introduced into the chambers between the anode and membrane, the membrane and the cathode. In the cathode part, a port drilled into the PTFE spacer is presented for an Ag/AgCl reference electrode to be positioned a specific distance from the working electrode. For a typical electrochemical test in flow cell, the electrolytes (0.1 M $KHCO_3$, 100 mL) were pre-saturated with N_2 or/and CO_2 with a rate of 50 mL min^{-1} for 30 min, the electrolyte were circulated through the cathode part and returned back to the reservoir using peristaltic pumps. The electrolyte flow was maintained at 10 mL min^{-1}. The gas flow rate was kept constant at 30 mL min^{-1} using a mass flow controller during the whole electrocatalytic process. The gas flow with the same rate was also circulated in the gas flow channel and the outlet was linked to a GC instrument for the quantification of gaseous products. The electrolyte in reservoir was extracted for further identification and quantification after electrochemical test.

Product quantification and identification. The identification and quantification of urea and NH_3 were achieved by NMR spectroscopy. For the identification and quantification of NH_3 from NRR, the extracted electrolyte was acidized to reach the pH value of *ca.* 3 by addition of appropriate amount of 0.5 M H_2SO_4 and a known

amount of d6-DMSO was used as an internal standard. The NMR spectrum was collected on an Ascend^{TM} 600 Nuclear Magnetic Resonance Spectrometer equipped with an ultralow temperature probe with the accumulation times of 2048. The full representative NMR spectra were displayed in Supplementary Figure 22. The same conditions were adapted to the measurements of standard solutions.

For the identification and quantification of urea and NH_3 simultaneously from electrocatalytic coupling reactions, the slow hydrolysis of urea to release NH_3 in an acid environment must be considered due to the relatively long time taken for data acquisition. The extracted electrolyte was initially subjected to the identification and quantification of urea without any post-process. And then, the product urea was reacted with diacetyl monoxime to generate an acid resistant chemical. Subsequently, the pH value of this solution was then adjusted to *ca.* 3 by addition of appropriate amounts of alkaline solution, and the containing ammonia was identified and quantified. The isotope labelled products possess the obviously differences in peak positions and characterizations compared to the unmarked ones, as illustrated in Supplementary Figs. 35 and 36. Based on this, the products of urea and ammonia from electrocatalytic process could be identified. The concentration of urea or ammonia exhibits a linear relationship with the integral area of the characteristic peaks, thus the concentration of products could be calculated via the equation of calibration curves.

The concentration of urea in the electrolyte was also measured by diacetyl monoxime method. With heating, the reaction between the diacetyl monoxime and urea in acid would generate a pink product and reaches the highest absorbance at 525 nm[45]. There is a linear relationship between the absorbance and the concentration of urea and the concentration of urea after electrochemical test was acquired according to the calibration curve (Supplementary Fig. 37). Likewise, the concentration of NH_3 and N_2H_4 were also quantified by the indophenols blue method[6] and the method of Watt and Chrisp[62] respectively, as seen in Supplementary Figs. 38 and 39.

The Faradic efficiency is the ratio of the number of electrons transferred for the formation of urea to the total amount of electricity that flow through the circuit. Assuming six electrons were needed to form one urea ($CO(NH_2)_2$) molecule, the Faradic efficiency for urea synthesis (FE) can be calculated as follows:

$$FE\ (\%) = (6 \times F \times C \times V)/(60.06 \times Q) \times 100$$

The amount of urea (m) was calculated by the equation:

$$m=C\times V$$

where F is the Faraday constant, Q is the electric quantity, C is the concentration of generated urea and V is the volume of the electrolyte. The formation rate of urea was averaged by the time and the presented urea formation rate is the average value within the time frame of the tests.

Isotope-labelling product quantification and identification. The isotope-labelling experiments for the identification of the products were carried out with labelled gases as feedstocks[63] ($^{15}N_2$ 98% Enrichment; $^{13}CO_2$ 99% Enrichment, Sigma). The electrochemical ammonia synthesis was performed on Pd_1Cu_1/TiO_2-400 under nitrogen gas ($^{14}N_2$ and $^{15}N_2$ respectively) in a flow cell. The yield rate of ammonia was 2.91 mmol g^{-1} h^{-1} at -0.4 V versus RHE for $^{14}N_2$, and a comparable value of 2.89 mmol g^{-1} h^{-1} was obtained for $^{15}N_2$ (Supplementary Fig. 35). The yielded ammonia exhibits distinguishing characteristics in the NMR spectra (triplet peaks for $^{14}NH_3$ and doublet peaks for $^{15}NH_3$)[6]. Moreover, a negligible yield rate (0.05 mmol g^{-1} h^{-1}) was obtained in an Ar atmosphere. The results indicated the high electrocatalytic activity of Pd_1Cu_1/TiO_2-400 towards the NRR and confirmed that ammonia was produced by electrocatalysis rather than contamination.

The tests were conducted with N_2 and CO_2 as feedstocks, and the concentrations of ammonia and urea were both quantified by NMR. The catalyst exhibited very similar catalytic activity and selectivity for urea synthesis (relatively low yield for ammonia) in $^{12}CO_2$ and $^{14}N_2$ or $^{13}CO_2$ and $^{15}N_2$, and the isotope labelled product can be intuitively distinguished due to the differences in peaks. The control experiments further proved the occurrence of electrochemical urea synthesis (Supplementary Fig. 36). It is equally important that the product urea was identified by gas chromatography-mass spectrometry (GC-MS). Trimethylsilyloxypyrimidine was obtained by derivatization (Fig. 2f) and subjected to GC-MS characterization due to the low decomposition temperature of urea. Compared with the main fragments of 153 and 168 for the unmarked product, the isotope labelled product displayed main fragments of 156 and 171, revealing that the carbon and nitrogen in the product were both derived from gaseous molecules and that the carbon was barely derived from the bicarbonate electrolyte.

The urea formation rates quantified by the diacetyl monoxime method are comparable to those quantified by NMR (Supplementary Fig. 40), indicating the applicability of quantification by these two methods. Moreover, the electrochemical tests were carried out in H cell with the addition of 100 ppm of NH_4HCO_3, and CO_2

alone served as the feeding gas; however, only negligible amounts of urea were obtained, indicating that the generated urea was not derived from ammonia by an electrocatalytic process or contamination. Additionally, when the ammonium salt was replaced by $HCOONH_4$ or CH_3COONH_4 and the feeding gas was substituted by N_2, only trace amounts of urea were obtained, thus excluding the generation of formic or acetate as an intermediate process in urea synthesis (Supplementary Fig. 41). Electrochemical stability is crucial for further application of electrocatalysts. The urea formation rate and Faradic efficiency remained stable over 6 cycles of electrocatalysis (Supplementary Fig. 42) in the H cell, and there was no obvious decay of the current density during electrocatalysis for 12 h (Supplementary Fig. 43), which also indicated the high electrochemical stability of Pd_1Cu_1/TiO_2-400.

Mass spectra measurement. 600 μL of electrolyte after electrochemical test was extracted, followed by addition of 20 μL of 1,1,3,3-Tetramethoxypropane aqueous solution (0.3 mol L^{-1}) and 40 μL of diluted hydrochloric acid (250 g L^{-1}). Then, the mixture reacted on the shake bed for 1 h at room temperature. The above product was further freeze-dried. After that, 200 μL of anhydrous acetonitrile was added into the reactor followed by addition of 20 μL of N-Methyl-N-(trimethylsilyl)trifluoroacetamide (MSTFA). After reaction for another 1 h at 60 °C, the final product of 2-trimethylsilyloxypyrimidine was analyzed on a GCMS-QP2020 NX spectrometer (Shimadzu).

Computational method. The DFT computations were performed via the plane-wave technique implemented in Vienna *ab initio* simulation package (VASP)[64]. The ion-electron interaction was described using the projector-augmented plane wave (PAW) approach[65]. The generalized gradient approximation (GGA) expressed by PBE functional[66] and a 460 eV cutoff for the plane-wave basis set were adopted in all computations. We created a 4×4 supercell to simulate the Pd-Cu surfaces and adopted a vacuum length of 20 Å in the *z* direction to avoid the longitudinal interlayer interaction. The geometry optimizations were performed using the conjugated gradient method and the convergence threshold was set to be 10^{-5} eV in energy and 10^{-4} eV $Å^{-1}$ in force. The Brillouin zone was represented by a Monkhorst-Pack special *k*-point mesh of 4 × 4 × 1 for geometrical optimizations. The climbing image nudged elastic band (CI-NEB)[67] method was implemented to simulate the *NCON* intermediate formation pathway. The deformation charge densities were performed via following equation:

$$\Delta\rho = \rho_{total} - \rho_{Cu} - \rho_{Pd}$$

where the ρ_{total}, ρ_{Cu}, ρ_{Pd} represent the charge density of Pd-Cu system, Cu and Pd respectively. The free energy of each reduction step can be obtained at zero bias potential using:

$$\Delta G = \Delta E + \Delta E_{ZPE} + T\Delta S$$

where ΔE is the reaction energy, ΔE_{ZPE} is the difference in zero point energies, T is the temperature (298.15 K), and ΔS is the reaction entropy. For absorbates, E_{ZPE} and S were determined by vibrational frequencies calculations with a low-frequency cutoff of ~45 cm^{-1}, where all 3N degrees of freedom were treated as harmonic vibrational motions without considering contributions from the slab. The gaseous molecules were treated as ideal gas and their thermochemistry data were taken from the NIST database[68].

References

62. Watt, G. W. & Chrisp, J. D. Spectrophotometric method for determination of hydrazine. *Anal. Chem.* **24**, 2006-2008 (1952).
63. Andersen, S. Z. et al. A rigorous electrochemical ammonia synthesis protocol with quantitative isotope measurements. *Nature* **570**, 504-508 (2019).
64. Kresse, G. & Furthmüller, J. Efficient iterative schemes for ab initio total-energy calculations using a plane-wave basis set. *Phys. Rev. B* **54**, 11169 (1996).
65. Blöchl, P. E. Projector augmented-wave method. *Phys. Rev. B* **24**, 17953 (1994).
66. Perdew, J. P., Burke, K. & Ernzerhof, M. Generalized gradient approximation made simple. *Phys. Rev. Lett.* **77**, 3865 (1996).
67. Henkelman, G., Uberuaga, B. P. & Jónsson, H. A climbing image nudged elastic band method for finding saddle points and minimum energy paths. *J. Chem. Phys.* **113**, 9901-9904(2000).
68. Johnson III, R. D. Computational chemistry comparison and benchmark database. http://cccbdb.nist.gov/ (2016).

Data availability

The datasets generated during and/or analysed during the current study are available from the corresponding author on reasonable request.

Code availability

The computational codes used in the current work are available from the corresponding author on reasonable request.

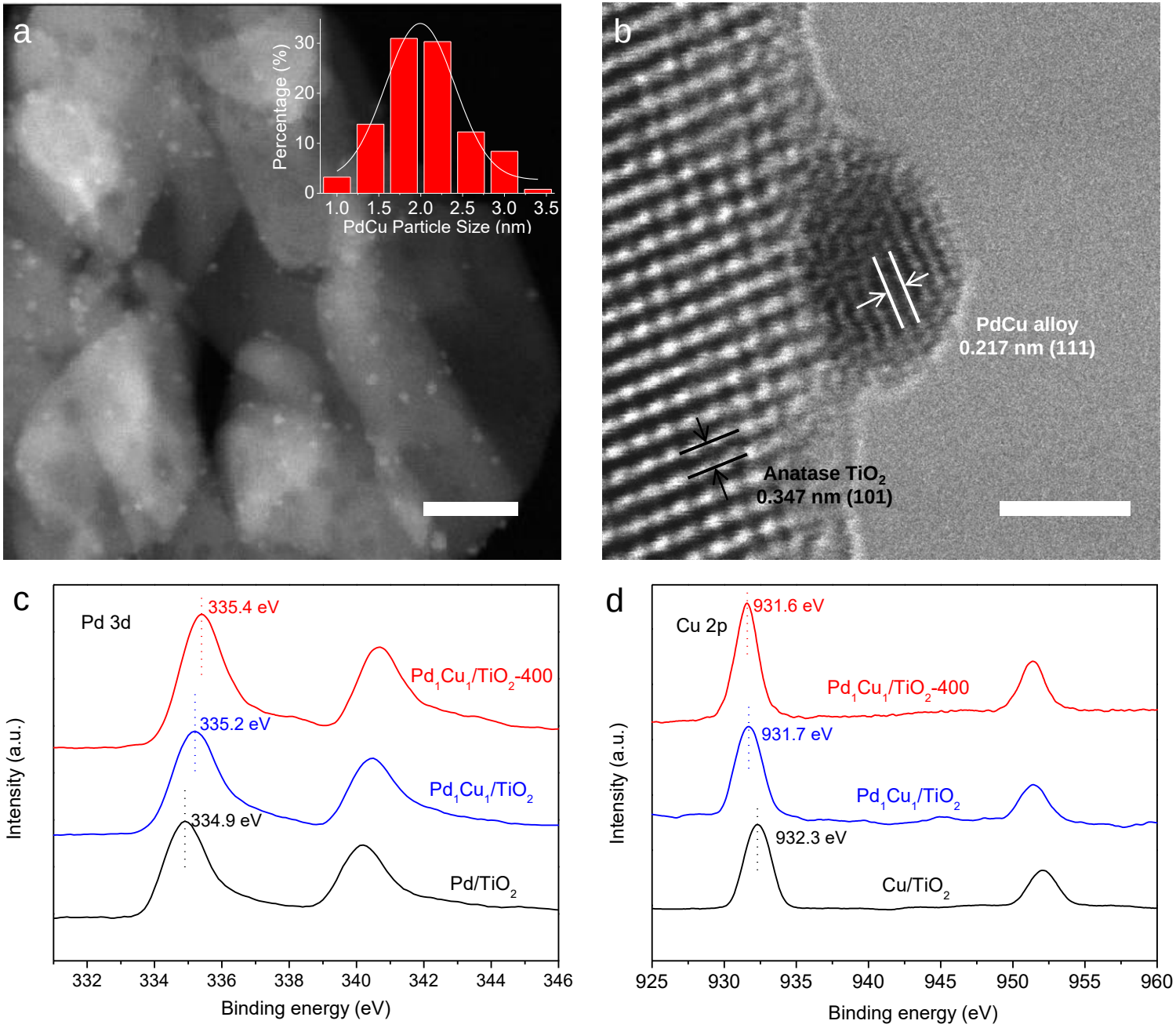
a
Percentage (%)
0
10
20
30
1.0
1.5
2.0
2.5
3.0
3.5
PdCu Particle Size (nm)
b
PdCu alloy
0.217 nm (111)
Anatase TiO2
0.347 nm (101)
c
Pd 3d
335.4 eV
Pd1Cu1/TiO2-400
335.2 eV
Pd1Cu1/TiO2
334.9 eV
Pd/TiO2
Intensity (a.u.)
332
334
336
338
340
342
344
346
Binding energy (eV)
d
Cu 2p
931.6 eV
Pd1Cu1/TiO2-400
931.7 eV
Pd1Cu1/TiO2
932.3 eV
Cu/TiO2
Intensity (a.u.)
925
930
935
940
945
950
955
960
Binding energy (eV)

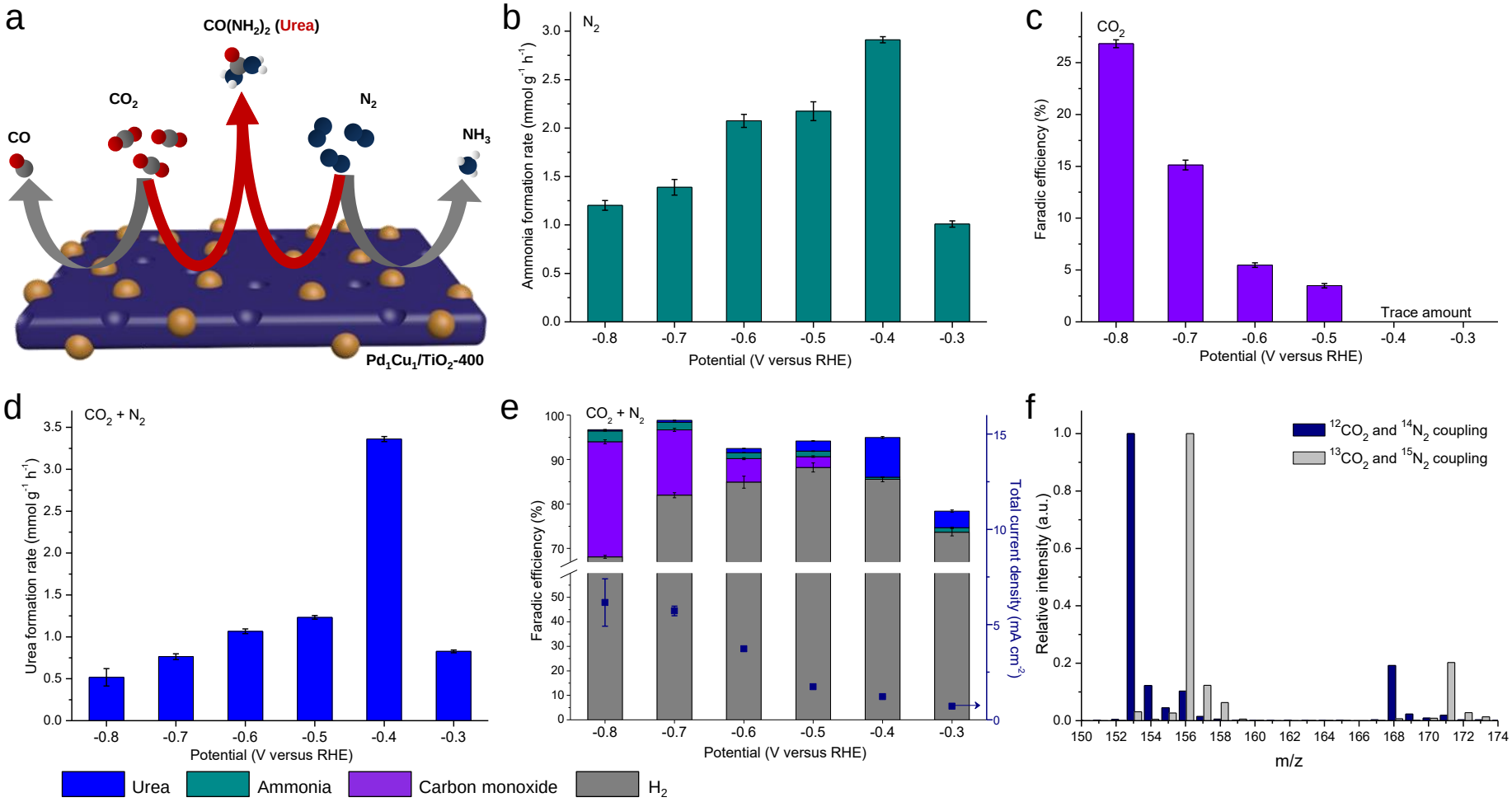
a
CO(NH2)2 (Urea)
CO2
N2
CO
NH3
Pd1Cu1/TiO2-400
b
N2
Ammonia formation rate (mmol g-1 h-1)
Potential (V versus RHE)
c
CO2
Faradic efficiency (%)
Trace amount
Potential (V versus RHE)
d
CO2 + N2
Urea formation rate (mmol g-1 h-1)
Potential (V versus RHE)
e
CO2 + N2
Faradic efficiency (%)
Total current density (mA cm-2)
Potential (V versus RHE)
f
12CO2 and 14N2 coupling
13CO2 and 15N2 coupling
Relative intensity (a.u.)
m/z
Urea
Ammonia
Carbon monoxide
H2

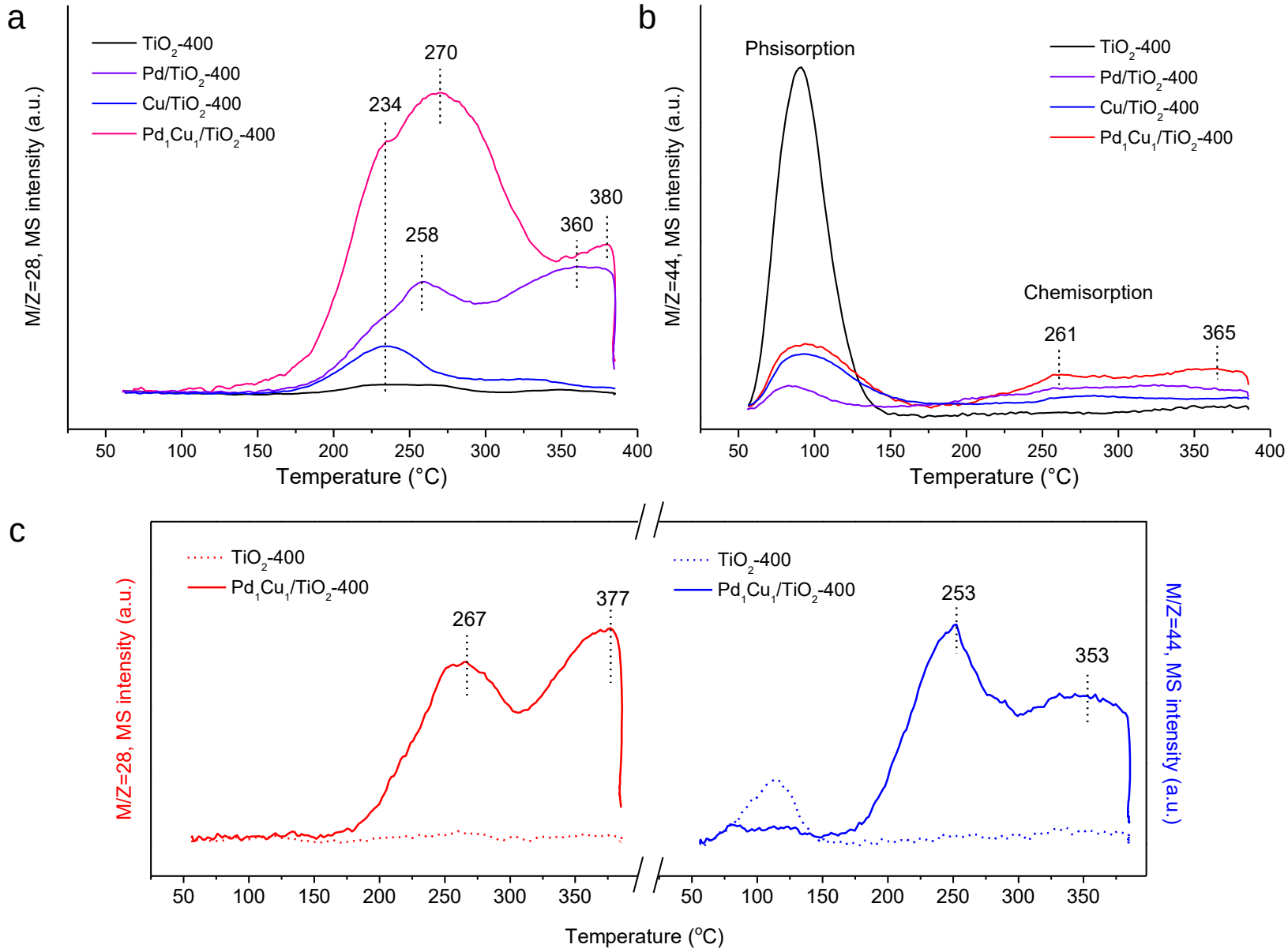
a
TiO2-400
Pd/TiO2-400
Cu/TiO2-400
Pd1Cu1/TiO2-400
270
234
258
380
360
M/Z=28, MS intensity (a.u.)
Temperature (°C)
b
Phsisorption
Chemisorption
261
365
M/Z=44, MS intensity (a.u.)
Temperature (°C)
c
267
377
253
353
M/Z=28, MS intensity (a.u.)
M/Z=44, MS intensity (a.u.)
Temperature (°C)

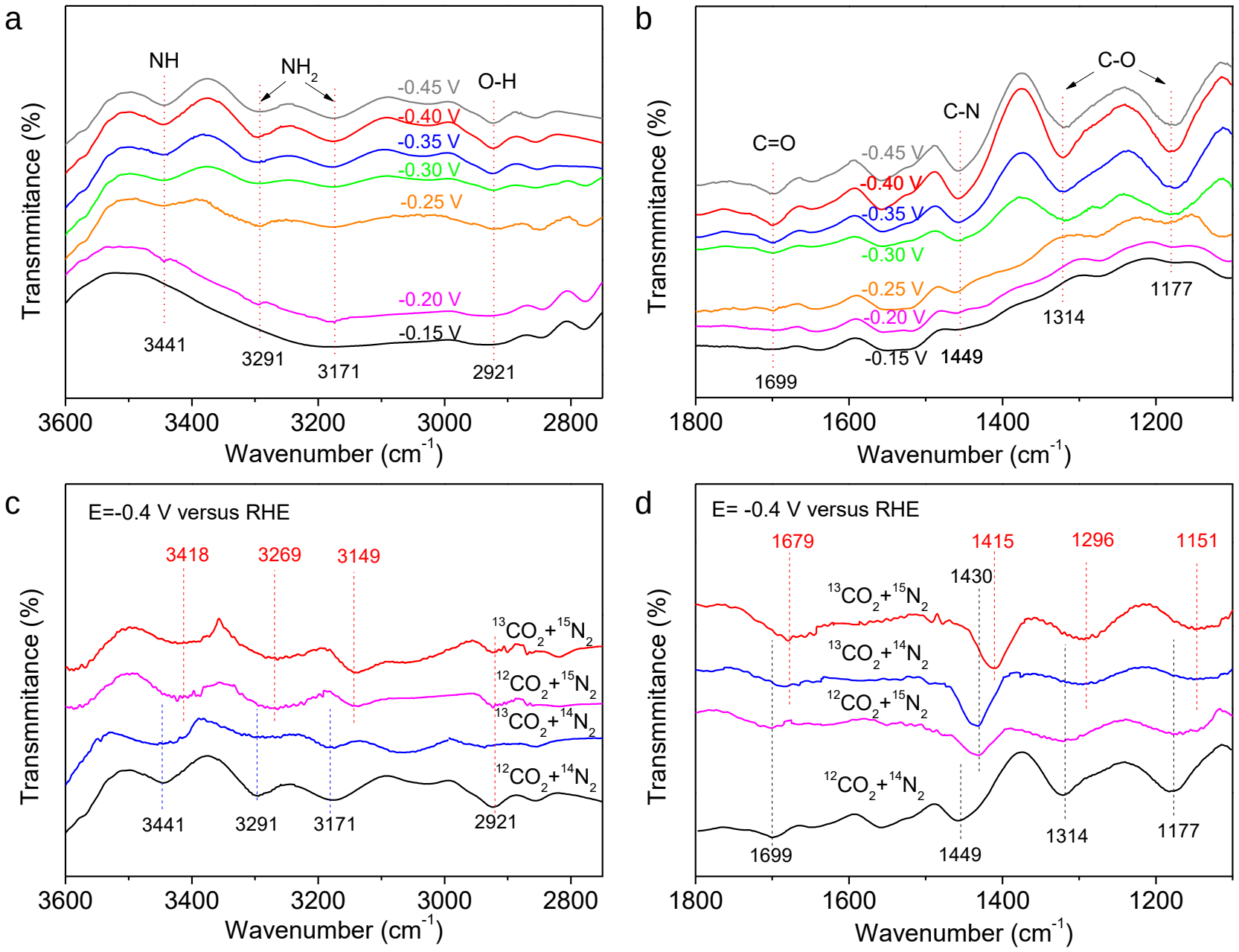
a
NH
NH2
O-H
-0.45 V
-0.40 V
-0.35 V
-0.30 V
-0.25 V
-0.20 V
-0.15 V
3441
3291
3171
2921
Transmmitance (%)
Wavenumber (cm-1)
b
C=O
C-N
C-O
1699
1449
1314
1177
c
E=-0.4 V versus RHE
3418
3269
3149
13CO2+15N2
12CO2+15N2
13CO2+14N2
12CO2+14N2
d
E= -0.4 V versus RHE
1679
1415
1296
1151
1430

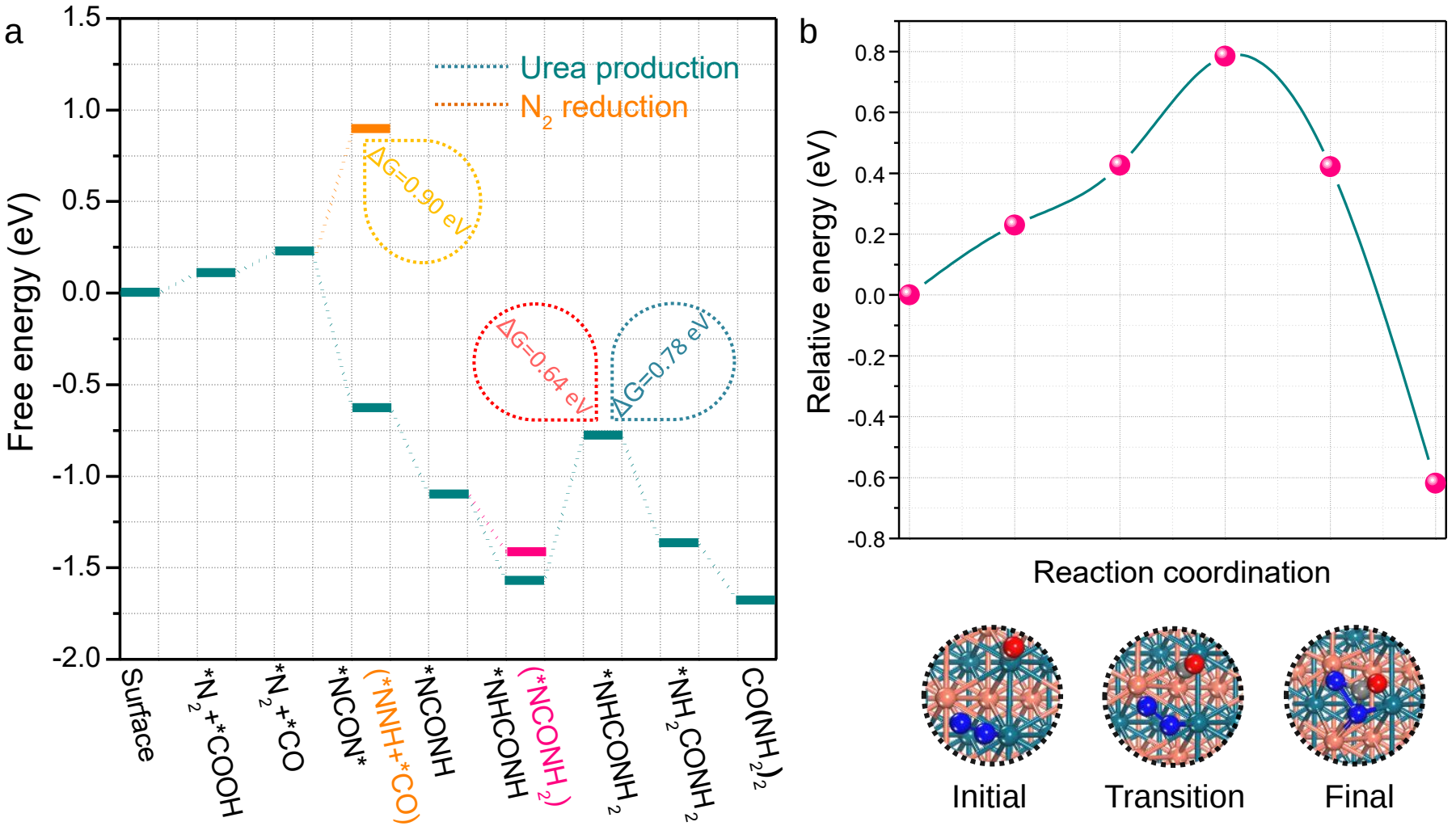
a
Free energy (eV)
1.5
1.0
0.5
0.0
-0.5
-1.0
-1.5
-2.0
Urea production
N2 reduction
ΔG=0.90 eV
ΔG=0.64 eV
ΔG=0.78 eV
Surface
*N2+*COOH
*N2+*CO
NCON
(*NNH+*CO)
*NCONH
*NHCONH
(*NCONH2)
*NHCONH2
*NH2CONH2
CO(NH2)2
b
Relative energy (eV)
0.8
0.6
0.4
0.2
0.0
-0.2
-0.4
-0.6
-0.8
Reaction coordination
Initial
Transition
Final